Available online at www.sciencedirect.com

SCIENCE DIRECT®

Remote Sensing of Environment 98 (2005) 237 – 250

Remote Sensing of Environment

www.elsevier.com/locate/rse

A comparison of methods for estimating fractional green vegetation cover within a desert-to-upland transition zone in central New Mexico, USA

Jingfeng Xiao [a,*], Aaron Moody [b]

[a] Department of Geography, University of North Carolina at Chapel Hill, Chapel Hill, NC 27599-3220, USA
[b] Department of Geography and Curriculum in Ecology, University of North Carolina at Chapel Hill, Chapel Hill, NC 27599-3220, USA

Received 24 December 2004; received in revised form 19 July 2005; accepted 22 July 2005

Abstract

We compared a set of methods for estimating fractional green vegetation cover (f_c) over a ~4000 km^2 region of central New Mexico, USA. The models used were trained and tested independently using high-resolution, true-color orthoimagery with 0.3 m spatial resolution. Simple NDVI-based methods performed well for estimating f_c regionally but overestimated f_c in sparsely vegetated areas with bright soils, and areas with abundant non-photosynthetic vegetation (e.g. dry shrubs). Three-, four-, and five-endmember spectral mixture models (SMA3, SMA4, and SMA5) were also compared. Constrained versions of these models all produced similar accuracy regionally, but constrained and unconstrained versions of the SMA5 model best captured f_c for the rarer landscapes (bright soils, riparian vegetation) found throughout the region. This indicates that heterogeneous landscapes can be stratified into relatively homogeneous strata, and three or four endmembers may be adequate to characterize the spectral variability within each stratum. Including NDVI along with the six reflective bands of ETM+ data, provided enough data dimensionality to support the five-endmember SMA model. This permitted a more complete representation of the range of spectral landscape types that are germane for separating out green vegetation in this semi-arid region. We also note that green woody vegetation and green grass cover should be spectrally represented by two different endmembers in SMA because these two vegetation types are spectrally different, particularly in the near-infrared (NIR) wavelength.

Keywords: Spectral mixture analysis; Fractional green vegetation cover; NDVI; Semi-arid; Landsat

1. Introduction

Vegetation plays an important role in the exchanges of carbon, water, and energy at the land surface (Hoffmann & Jackson, 2000; Nemani & Running, 1996; Schimel et al., 2001; Tueller, 1987; Ward & Robinson, 2000). Thus, fractional green vegetation cover (f_c) is an important element of models that attempt to account for these exchanges (Deardorff, 1978; Gutman & Ignatov, 1998; Hirano et al., 2004; Wittich & Hansing, 1995; Zeng et al., 2002). f_c is also a sensitive indicator of land degradation and desertification in arid and semi-arid regions and, if easily measured, can be used to study these processes (Purevdorj et al., 1998). Remote sensing provides a seemingly obvious data source for quantifying f_c over large areas. However, most remote sensing data are too coarse for the direct measurement of f_c.

On arid and semi-arid lands, vegetation is often sparsely distributed, and even relatively fine-resolution remote sensing data (e.g. 30×30 m data from Landsat) contain spectra that result from the mixed reflectance of vegetation, bare soil, and shadow. Thus, units of vegetation are not individually resolved. Spectral mixture analysis (SMA) has often been used to estimate subpixel canopy proportions from multispectral satellite data (Adams et al., 1995; Rashed et al., 2003; Roberts et al., 1998; Small, 2001, 2003; Wu & Murray, 2003). Good results have been achieved using three-and four-endmember models, and methods based on the normalized difference vegetation index (NDVI), including a two-endmember SMA model (Gutman & Ignatov, 1998; Qi et al., 2000; Wittich & Hansing, 1995) and a simple regression method (Elmore et al., 2000; Hurcom & Harrison, 1998).

* Corresponding author. Tel.: +1 919 962 3871.
E-mail address: jfxiao@email.unc.edu (J. Xiao).

0034-4257/$ - see front matter © 2005 Elsevier Inc. All rights reserved.
doi:10.1016/j.rse.2005.07.011

Most of these methods have been applied to arid and semi-arid environments (e.g. Asner & Heidebrecht, 2002; Elmore et al., 2000; Qi et al., 2000; Smith et al., 1990) but, to our knowledge, their relative accuracy has not been quantitatively evaluated.

The number of endmembers included in SMA is constrained by the dimensionality of the satellite image to which the model is applied (Theseira et al., 2002). For Landsat data, a maximum of four endmembers are usually used because the three visible bands are strongly correlated with each other (Small, 2001; Theseira et al., 2002). However, four endmembers may still be inadequate to spectrally characterize the complex and heterogeneous landscapes in semi-arid regions. The use of more than four endmembers in a single mixture model for Landsat data has received little attention.

We compared three-, four-, and five-endmember SMA models, the NDVI-based SMA model, and the simple NDVI-based regression model for estimating f_c in a heterogeneous, semi-arid region (Albuquerque, New Mexico) from Landsat ETM+ data. These models were calibrated and statistically evaluated using spatially independent data sets of vegetation fraction derived from high-resolution orthoimagery. Our objective was to evaluate how the properties of the mixture model used to estimate f_c affected the accuracy of the model estimates in this heterogeneous, semi-arid environment.

2. Background

It is commonly noted that reflectance spectra derived from satellite-based sensors constitute mixed signals, in particular when the sizes of scene objects are smaller than the instantaneous field of view (Graetz & Gentle, 1982; Pech et al., 1986; Strahler et al., 1986). This phenomenon is prevalent in arid and semi-arid regions at the resolution of Landsat data (30 $\times$30 m), even for the basic separation of vegetated and unvegetated lands, because the density of vegetation is often low, and woody plants tend to be dispersed spatially (Elmore et al., 2000). The most common approach for characterizing ground cover at the sub-pixel scale using remote sensing data is SMA (Adams et al., 1995, 1986; Smith et al., 1990) although other methods have also been used, including artificial neural networks (Atkinson et al., 1997; Pu et al., 2003), fuzzy classifiers (Foody, 1996), maximum likelihood classifiers (Foody et al., 1992; Häme et al., 2001), regression trees (DeFries et al., 1997; Yang et al., 2003), decision trees (McIver & Friedl, 2002), and simple regression based on NDVI (Elmore et al., 2000).

An important assumption of linear SMA is that the spectral signature of a given pixel is the linear, proportion-weighted combination of the endmember spectra (Smith et al., 1990). An endmember is a pure surface material or land-cover type that is assumed to have a unique spectral signature (referred to as the endmember signature). The spectral variability within an endmember is usually assumed to be minimal or negligible. The selection of endmembers is critical for the success of a mixture model. Endmember signatures can be directly selected from the image (image endmembers), or extracted from field or laboratory spectra of known materials (reference endmembers) (Adams et al., 1995). There are numerous approaches for deriving image endmembers (e.g. see Boardman et al., 1995; Oki et al., 2002; Rashed et al., 2003; Small, 2003; Tompkins et al., 1997; Wu & Murray, 2003) including the use of two-dimensional feature space plots (Peterson & Stow, 2003) and identification of pure pixels with reference to field data or higher-resolution remote sensing data (Shoshany & Svoray, 2002). We combined these latter two approaches in this study.

Although several studies have demonstrated and modeled nonlinear spectral mixing between vegetation and soil (e.g., Borel & Gerstl, 1994; Huete, 1986; Huete et al., 1985; Ray & Murray, 1996) the effects of multiple scattering or nonlinear mixing are assumed to be negligible in most SMA applications, and linear SMA models have proven reasonably effective in estimating endmember fractions (Adams et al., 1986, 1995; Elmore et al., 2000; Small, 2001, 2003; Smith et al., 1990; Theseira et al., 2002). In general, linear models are more widely used due to their simplicity, reasonable effectiveness and interpretability. The majority of linear SMA modeling applications are restricted to three or four endmembers due to the dimensionality of Landsat data on which most SMA analyses have been based (e.g., Adams et al., 1995; Asner & Heidebrecht, 2002; Elmore et al., 2000; Small, 2001, 2003).

A highly-simplified SMA model is the two-endmember model based on NDVI (Wittich & Hansing, 1995), referred to as the NDVI–SMA model hereafter. NDVI–SMA assumes that a given pixel consists of only green vegetation and bare soil, and thus its NDVI value is the linear combination of contributions from these two components (Gutman & Ignatov, 1998; Qi et al., 2000; Wittich & Hansing, 1995). With only two endmembers, NDVI–SMA consists of a single equation, which simplifies the endmember selection process and substantially improves computational efficiency. This model has been applied to estimate f_c at both regional and global scales (Gutman & Ignatov, 1998; Qi et al., 2000; Wittich & Hansing, 1995; Zeng et al., 2000).

Regression relations between NDVI and known vegetation abundance have also been used to estimate f_c (Elmore et al., 2000; García-Haro et al., 1996; Hurcom & Harrison, 1998). This method is referred to as the NDVI-regression method below. Hurcom and Harrison (1998) showed that NDVI provides a reliable and efficient measure of vegetation abundance. However, laboratory analyses have shown that vegetation fraction estimates based on spectral mixture modeling are less sensitive to background soil reflectance than those estimated using the NDVI-regression method (Elmore et al., 2000; García-Haro et al., 1996). In this paper, we evaluated the relative accuracy of three-, four-, and five-endmember SMA models (SMA3, SMA4, and SMA5, respectively), and the NDVI–SMA and NDVI-regression methods for estimating f_c within the range of cover present

along a gradient from semi-desert scrub to southwestern montane forest in an area near Albuquerque, New Mexico.

3. Study region

This study was conducted over an area of approximately 3690 km^2 located in central New Mexico (Fig. 1). Wide valleys in this region are sparsely vegetated (about 0–20%), primarily occupied by desert grassland, and open shrubland, with occasional woodlands of varying density. High elevation mountainous areas are dominated by montane coniferous forest, generally descending through zones of montane scrub, coniferous and mixed woodland, juniper savanna, and plains-mesa sand scrub (Earth Data Analysis Center, 1991). Mean annual temperature is 11.87 °C over the region, but local values vary along an elevation gradient from 2.69 to 13.72 °C. Likewise, average annual precipitation is 324 mm, but ranges from 220 to 758 mm across the region. Precipitation is of monsoonal origin and the rainy season lasts from July to October. The rest of the year is generally dry except at higher elevations.

Coniferous forest, coniferous woodland, and juniper savanna are dominated by evergreen plants, which retain photosynthetic tissue during the dry season. Shrubs are sparsely distributed in flat areas and foothills, whereas trees are more densely distributed in the mountainous areas. Annual and perennial grasses and herbs emerge at the onset of the rainy season and senesce shortly after its conclusion, although herbaceous vegetation (primarily grass and crops) may also be emergent in riparian and urban areas during the dry season. Urban areas (Albuquerque) were not included in the analysis.

4. Data

The dates of the remote sensing imagery used for this study coincide temporally, and fall within a period of the growing season (March) when the scene components of interest are most spectrally separable. In March, green vegetation primarily includes evergreen trees and shrubs. Herbaceous vegetation in riparian areas has a higher reflectance than evergreen woody vegetation, particularly in the near-infrared wavelength, and could thus be treated as a separate endmember in our analysis.

4.1. High-resolution orthoimagery

True-color high-resolution (0.3 m) orthoimagery was acquired in March, 2002, and is available from the USGS (http://seamless.usgs.gov). We used these data to produce training and validation datasets for developing and evaluating mixture models. The orthoimagery was available for most of the study region (Fig. 1).

4.2. Landsat data and processing

All the methods described above were performed using a cloud-free Landsat ETM+ image (Path 33, Row 36) acquired on March 28, 2002. The Landsat ETM+ image consists of six reflective bands (30 m), one thermal band (60 m), and one panchromatic band (15 m). The six reflective bands were used in our study.

The Landsat ETM+ image was georeferenced using sixty-four ground control points (GCP) selected with reference to 1:24,000 USGS topographic maps. The geometric correction was performed using a first-order trans-

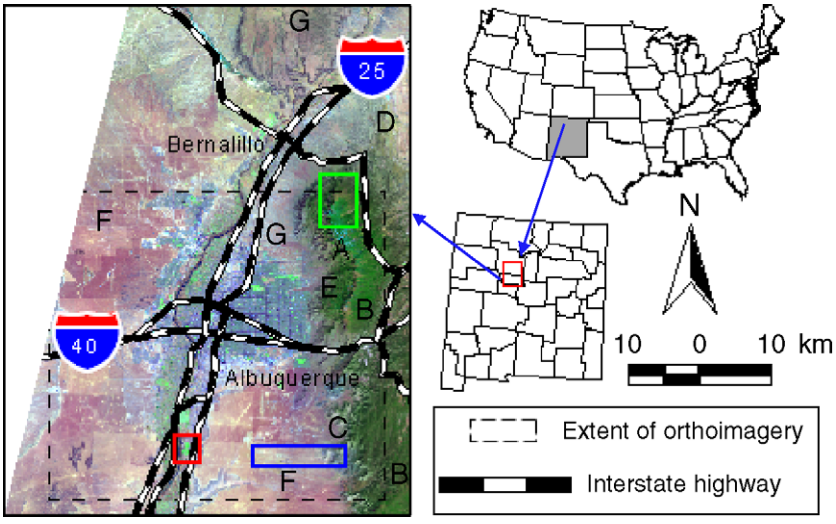

Fig. 1. Location of the study region in central New Mexico. A wide variety of natural vegetation types are distributed in this region: subalpine coniferous forest (A), montane coniferous forest (B), coniferous and mixed woodland (C), juniper savanna (D), montane scrub (E), plains-mesa sand scrub (F), and desert grassland (G). The green indicates a *NPV*-dominated area. The left portion of the area delineated by the blue rectangle is a barren area where the soil background is dominated by light soil. The red rectangle indicates riparian grass (*Green Vegetation 1*). (For interpretation of the references to colour in this figure legend, the reader is referred to the web version of this article.)

formation with an overall root-mean-squared error (RMSE) of between 0.3 and 0.4 pixel.

The digital number (DN) values of the geometrically-corrected ETM+ data were converted to at-satellite radiance using the following equation (Markham & Barker, 1987; Price, 1987):

$$L_\lambda = ((\mathrm{LMAX}_\lambda - \mathrm{LMIN}_\lambda)/(\mathrm{QCALMAX} - \mathrm{QCALMIN})) \times (\mathrm{QCAL} - \mathrm{QCALMIN}) + \mathrm{LMIN}_\lambda \quad (1)$$

where L_λ is at-satellite radiance (W m^{-2} sr^{-1} μm^{-1}), QCAL=DN, LMAX_λ and LMIN_λ are the spectral radiances that are scaled to QCALMAX and QCALMIN in W m^{-2} sr^{-1} μm^{-1}, respectively, QCALMAX=255, and QCALMIN=1.

At-satellite radiances were then converted to surface reflectance by correcting for both solar and atmospheric effects. The general equation for converting at-satellite radiance to surface reflectance (Moran et al., 1992) is:

$$\rho = \frac{\pi(L_s - L_d)}{\tau_v(E_0 \cos\theta_z \tau_z + E_d)} \quad (2)$$

where ρ is the surface reflectance, L_s is the at-satellite radiance, L_d is the path radiance (W m^{-2} μm^{-1}), E_0 is the solar spectral irradiance (W m^{-2} μm^{-1}), θ_z is solar zenith angle, τ_v is the atmospheric transmittance along the path from the ground surface to the sensor, τ_z is the atmospheric transmittance along the path from the sun to the ground surface, and E_d is downward diffuse radiation (W m^{-2} μm^{-1}). We converted at-satellite radiance values to surface reflectance using a dark object subtraction (DOS) approach (Chavez, 1989) which assumes no atmospheric transmittance loss and no downward diffuse radiation. The surface reflectance of the dark object was assumed to be 1%, and thus the path radiance was assumed to be the dark-object radiance minus the radiance contributed by 1% surface reflectance (Moran et al., 1992). The DN of the dark object is often estimated from the ETM+ image using the lower bound of the histogram derived from each band (Moran et al., 1992). The DN value of the dark object here was selected as the darkest DN with at least a thousand pixels over the entire scene (McDonald et al., 1998; Teillet & Fedosejevs, 1995).

5. Methods

5.1. Spectral mixture analysis

The general form of the linear SMA is:

$$R_k = \sum_{i=1}^{M} f_i r_{i,k} + e_k \quad (3)$$

where R_k is the reflectance for each band (k), M is the number of endmembers, f_i is the fraction of endmember i, $r_{i,k}$ is the reflectance of endmember i at band k, and e_k is the residual term at band k. Model fit is usually assessed using the RMSE:

$$\mathrm{RMSE} = \left(\sum_{k=1}^{N} (e_k)^2/N\right)^{1/2} \quad (4)$$

where N is the number of bands, and e_k is the residual term at band k ($k=1,2,\ldots,N$).

The derived fractions of endmembers are often subject to the unity constraint:

$$\sum_{i=1}^{M} f_i = 1. \quad (5)$$

The Lagrange multiplier is used to incorporate the unity constraint into mixture models. Another constraint is that each endmember fraction should lie between 0.0 and 1.0. Fractions beyond this range are mathematically possible but physically unreasonable. A properly constructed SMA model should produce endmember fractions that meet this condition without the constraint (Elmore et al., 2000). Moreover, this additional constraint requires the incorporation of inequalities in a SMA model, which complicates the implementation of the model (e.g., Heinz & Chang, 2001).

For both three- and four-endmember SMA (SMA3 and SMA4), models were developed with and without the unity constraint in order to assess how the constraint affected the accuracy of vegetation fraction estimates. SMA models were tested with different combinations of endmembers. In each case, the endmember configuration that produced best results was adopted for comparison with other methods. These models were based on the six reflective bands of the ETM+ data.

5.2. NDVI-regression method

The NDVI-regression approach provides a simple solution to the estimation of f_c (e.g., Hurcom & Harrison, 1998). A regression model is first developed based on training data with known NDVI values and actual vegetation fractions. The model is then used to estimate vegetation fractions for all pixels across the image.

We randomly selected sixty pixels from the ETM+ image, and the orthoimagery was used to estimate the actual f_c within a 3×3 window around each sampled ETM+ pixel. Thus, for each sample (i.e., 3×3 window at ETM+ resolution), actual f_c was estimated from a corresponding 300×300 pixel subset from the 3-band, true-color orthoimagery.

Each orthoimagery subset was classified, using Bayesian maximum likelihood classification, into *Green Vegetation, Non-Photosynthetic Vegetation (NPV), Dark Soil, Light Soil, Water, Light Shadow*, and *Dark Shadow* (Fig. 2). Each orthoimagery subset was separately classified based on

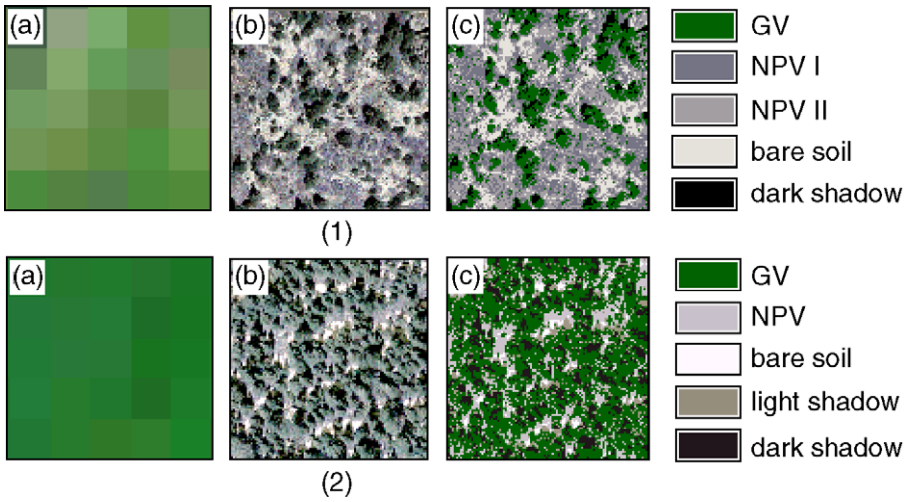

Fig. 2. The estimation of actual fractional green vegetation cover (f_c) within the 3×3 window surrounding each sample ETM+ pixel from the high-resolution orthoimagery. (1) An example for a sparsely vegetated window; (2) An example for a densely vegetated window. For each example, (a) is the ETM+ subset with 7–4–1 band combination (the red square represents the 3×3 window surrounding the sample ETM+ pixel); (b) is the orthoimagery subset corresponding to the 3×3 window as delineated by the red square in (a); (c) is the classified image of the orthoimagery subset. A legend is provided for each classified image. GV is the abbreviation for green vegetation. (For interpretation of the references to colour in this figure legend, the reader is referred to the web version of this article.)

training data selected from the subset. Dark shadows contained shaded canopy and shaded background, while light shadows were caused by topography or canopies. Dark shadows were equally partitioned to green vegetation and non-vegetation. The proportion of pixels classified as green vegetation (p) in each orthoimagery subset was calculated as:

$$p = (N_v/N) \times 100\% \quad (6)$$

where N_v is the total number of pixels classified as green vegetation, and N is the total number of pixels in the subset image. Thus, p is the approximation of the actual f_c within the 3×3 window surrounding each sampled ETM+ pixel.

The average NDVI value was extracted for each window from the ETM+ image, and linear regression model was used to model the relationship between actual f_c and NDVI for the sample pixels:

$$f_c = \beta_0 + \beta_1 \times \mathrm{NDVI} + \mathrm{error} \quad (7)$$

where β_0 is the intercept, and β_1 is the slope of the regression model. The linear regression model was used to estimate f_c for each pixel in the ETM+ image.

5.3. NDVI–SMA model

Deardorff (1978) expressed heat and moisture coefficients as linear functions of fractional vegetation cover. The general form of the linear relation is written as:

$$\phi = (1 - \sigma) \times \phi_{\sigma=0} + \sigma \times \phi_{\sigma=1} \quad (8)$$

where ϕ is the heat or moisture coefficient, $\phi_{\sigma=1}$ and $\phi_{\sigma=0}$ are contributions from vegetated ground and bare soil, respectively, and σ is fractional vegetation cover. Wittich and Hansing (1995) applied this general formulation to NDVI for the approximation of f_c:

$$\mathrm{NDVI} = f_c \times \mathrm{NDVI}_{veg} + (1 - f_c) \times \mathrm{NDVI}_{soil} \quad (9)$$

which can be rewritten as:

$$f_c = (\mathrm{NDVI} - \mathrm{NDVI}_{soil})/(\mathrm{NDVI}_{veg} - \mathrm{NDVI}_{soil}). \quad (10)$$

The NDVI value of the pixel has no subscript. NDVI_{veg} is the NDVI value of a pure green vegetation pixel, and NDVI_{soil} is the NDVI value of bare soil. We used the inversion of NDVI-regression to estimate NDVI_{veg} and NDVI_{soil} by assuming that *Green Vegetation* and *Bare Soil* have 100% and 0% vegetation, respectively. NDVI–SMA was then used to estimate vegetation fraction for each pixel in the ETM+ image.

NDVI–SMA is based on the assumption that the NDVI value of a given pixel is the linear combination of NDVI values of green vegetation and bare soil, weighted by their relative proportions. We examined the relationship between original NDVI values and NDVI_{mixed} in order to assess the validity of this assumption. The NDVI_{mixed} value of a given ETM+ pixel is calculated as:

$$\mathrm{NDVI}_{mixed} = F_c \times \mathrm{NDVI}_{veg} + (1 - F_c) \times \mathrm{NDVI}_{soil} \quad (11)$$

where F_c and $(1 - F_c)$ are the actual fractions of green vegetation and bare soil within the pixel, respectively.

5.4. Five-endmember SMA model

The number of endmembers used in SMA is constrained by the dimensionality of the satellite image that is used (Theseira et al., 2002). For example, for our study area, the correlation coefficients among the three visible bands of the

Landsat ETM+ data were 0.98 (band 1 and band 2), 0.94 (band 1 and band 3), and 0.98 (band 2 and band 3), illustrating that the dimensionality of these data is not as high as suggested by the spectral resolution. Thus, a maximum of four endmembers is usually used in SMA models using Landsat data (e.g., Adams et al., 1995; Elmore et al., 2000; Wu & Murray, 2003). However, four endmembers may be inadequate to characterize spectrally complex and heterogeneous landscapes.

NDVI captures the contrast between the visible-red and near-infrared reflectance of vegetation canopies, and is defined as:

$$\mathrm{NDVI} = (\mathrm{NIR} - \mathrm{RED})/(\mathrm{NIR} + \mathrm{RED}) \quad (12)$$

where NIR and RED are the visible-red (0.58–0.68 μm) and near-infrared (0.725–1.1 μm) wavelength regions, respectively. NDVI is strongly related to the fraction of photosynthetically active radiation (fPAR), and hence is closely associated with vegetation activity or greenness (e.g., Asrar et al., 1984; Myneni et al., 1995). In our study region, NDVI is moderately correlated with the red band ($R^2=0.40$), and only weakly related to the NIR band ($R^2=0.06$). Thus, there is no doubt that, as a nonlinear combination of red and NIR, NDVI provides new information that is linearly independent of the original red and NIR bands.

Including NDVI along with the six reflective bands resulted in a seven-band ETM+ image, which extended the dimensionality of the ETM+ data and allowed the use of five endmembers in a single SMA model. A five-endmember SMA model (SMA5) may lead to improved estimation of endmember fractions because the spectral variability of the study region can be better captured by using one more endmember in the unmixing analysis.

5.5. Endmember selection

For SMA3, SMA4, and SMA5 models, we derived endmember spectra from the ETM+ image. Six endmembers were selected, including *Green Vegetation I, Green Vegetation II, NPV, Dark Soil, Light Soil*, and *Shade*. The two-dimensional feature space plot between the red and NIR bands (Peterson & Stow, 2003) was used for the selection of endmembers. The upper-left apex of the feature space represents pure green vegetation in urban areas and riparian areas, including green grass and croplands. The upper-right apex is characterized by dry salt lakes with high reflectance values, which are not representative of the spectral signatures of soils in the study region. Thus, only green vegetation (*Green Vegetation I*) and *Shade* endmembers were selected from the feature space. Natural vegetation including coniferous forest and juniper savanna exhibited lower reflectance than riparian grass. Thus, another green vegetation endmember (*Green Vegetation II*) was selected from pure pixels that were identified from the ETM+ image with high-resolution orthoimagery. Other endmembers including *NPV*, *Dark Soil*, and *Light Soil* were also selected from pure pixels with reference to the orthoimagery. The spectral signatures of all selected endmembers are shown in Fig. 3.

With a total of six endmembers considered, there were 20 possible three-endmember combinations for SMA3 models, 15 possible four-endmember combinations for SMA4 models, and 6 possible five-endmember combinations for SMA5 models. For each model, all endmember combinations were explored, and the best endmember configuration as determined through visual interpretation of both RMSE and vegetation fraction maps was adopted for the model.

Unlike these models, NDVI–SMA has two fixed endmembers: green vegetation and bare soil. The NDVI values of these two endmembers ($\mathrm{NDVI}_{\mathrm{veg}}$ and $\mathrm{NDVI}_{\mathrm{soil}}$) were derived from the inversion of the NDVI-regression model (Eq. (7)) by assuming they had 100% and 0% green vegetation, respectively.

5.6. Validation

A total of 170 pixels were randomly selected from the ETM+ image for model validation. These sample pixels were spatially independent from those pixels used as training data for the development of NDVI-regression. A 3×3 window was used to account for coregistration errors between the ETM+ image and the orthoimagery. The high-resolution orthoimagery was used to estimate the actual f_c for the 3×3 window surrounding each sampled ETM+ pixel (see NDVI-regression method above). The resulting actual vegetation fractions of these sample ETM+ pixels were then compared with their predicted vegetation fractions for evaluation of each model. Coefficients of determination (R^2) and overall RMSE were both used to assess the accuracy of each method.

Narrowly distributed surface types including both *NPV*-dominated areas and sparsely vegetated areas with light soil

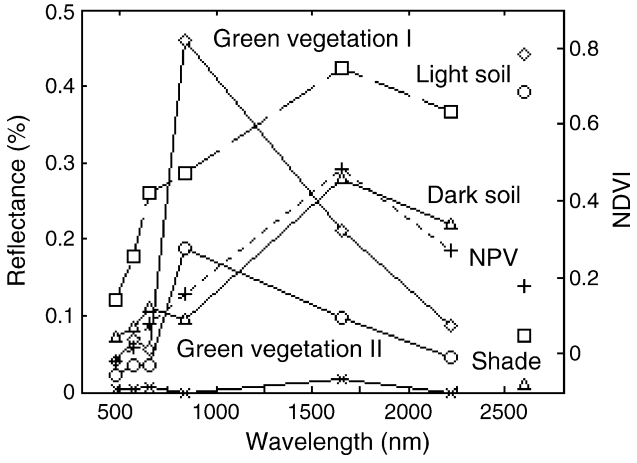

Fig. 3. ETM+-based spectral signatures of the six selected endmembers. The individual symbols represent NDVI values of endmembers: diamond (*Green Vegetation I*), circle (*Green Vegetation II*), plus sign (*NPV*), triangle-upward (*Dark Soil*), and square (*Light Soil*).

background were not well represented by the validation data as developed above. Thus, orthoimagery subsets and/or classified imagery were used to evaluate the accuracy of the different methods for estimating f_c for these narrowly distributed areas.

6. Results

The best SMA3 model was based on endmembers for *Green Vegetation II*, *Dark Soil*, and *Light Soil*. The unconstrained SMA3 model estimated f_c relatively well for less densely vegetated pixels (cover <40%) but substantially underestimated cover for densely vegetated pixels (cover >60%) (Fig. 4(a)). In contrast, the constrained model estimated f_c well for the full range of vegetation cover (Fig. 4(b)) thus producing higher accuracy than its unconstrained counterpart (Table 1). For *NPV*-dominated areas, however, both models substantially overestimated f_c although the constrained model still performed better than its unconstrained counterpart (Fig. 5). The overestimation of f_c in *NPV*-dominated areas was most likely because *NPV* was not included as an endmember in these models. Note that, although the spectra for *Dark Soil* and *NPV* were very similar (Fig. 3), the reflectance of *NPV* increased from the red to NIR wavelength, while the reflectance of *Dark Soil* decreased.

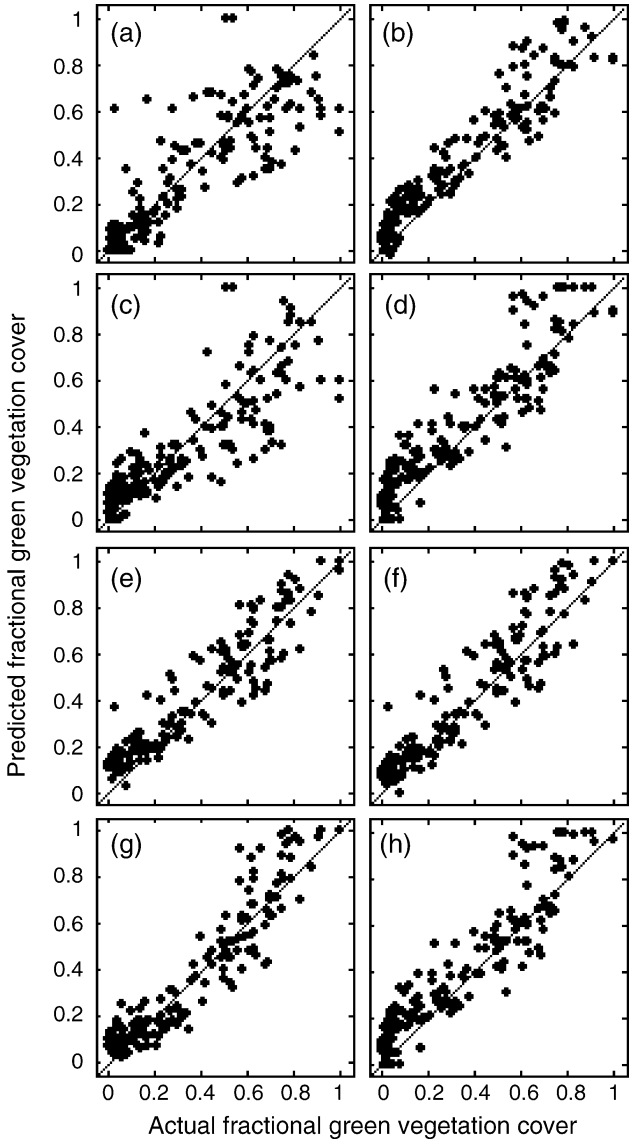

Fig. 4. Relationship between actual and predicted fractional green vegetation cover (f_c): (a) unconstrained SMA3; (b) constrained SMA3; (c) unconstrained SMA4; (d) constrained SMA4; (e) NDVI-regression; (f) NDVI–SMA; (g) unconstrained SMA5; (h) constrained SMA5. The solid line is the 1:1 line.

Table 1
R^2 and RMSE values between actual vegetation fraction and vegetation fraction predicted from each method

	SMA3		SMA4		NDVI		SMA5	
	U	C	U	C	NDVI-regression	NDVI–SMA	U	C
R^2	0.71	0.89	0.72	0.85	0.87	0.88	0.88	0.86
RMSE	0.159	0.099	0.150	0.123	0.105	0.106	0.100	0.118

All the linear relationships for the validation are statistically significant at $p<0.0001$. *Unconstrained* is denoted as U, and *constrained* is denoted as C.

The best SMA4 model included endmembers for *Green Vegetation II*, *NPV*, *Dark Soil*, and *Light Soil*. As with SMA3, the unconstrained SMA4 model strongly underestimated f_c when canopy cover exceeded about 40%, and the constrained version worked well across the range of fractions (Fig. 4(c), (d)). Note that the unconstrained SMA4 had slightly better accuracy than the unconstrained SMA3 model, and the constrained version performed as well as the SMA3. In *NPV*-dominated areas, however, both SMA4 models predicted f_c reasonably well (Fig. 5) likely because of the inclusion of the *NPV* endmember in these models.- There was a strong, linear relation between actual f_c and NDVI ($R^2=0.89$, $p<0.0001$). The linear regression model was written as:

$$f_c = 0.114 + 1.284 \times \mathrm{NDVI}. \quad (13)$$

The model was used to estimate f_c for each pixel in the ETM+ image. Predicted values of f_c, produced using the NDVI-regression method, also had a strong, linear relationship to actual vegetation fraction for the validation ETM+ pixels (Fig. 4(e)). The accuracy of the model was significantly higher than that of unconstrained SMA3 and SMA4 models, and comparable to that of constrained SMA3 and SMA4 models (Table 1). However, this method substantially overestimated f_c in *NPV*-dominated areas (Fig. 5) and sparsely vegetated or barren areas dominated by *Light Soil* (Fig. 6) because *NPV* and *Light Soil* both have slightly higher NDVI values than *Dark Soil*, which is the dominant background soil type across the region.

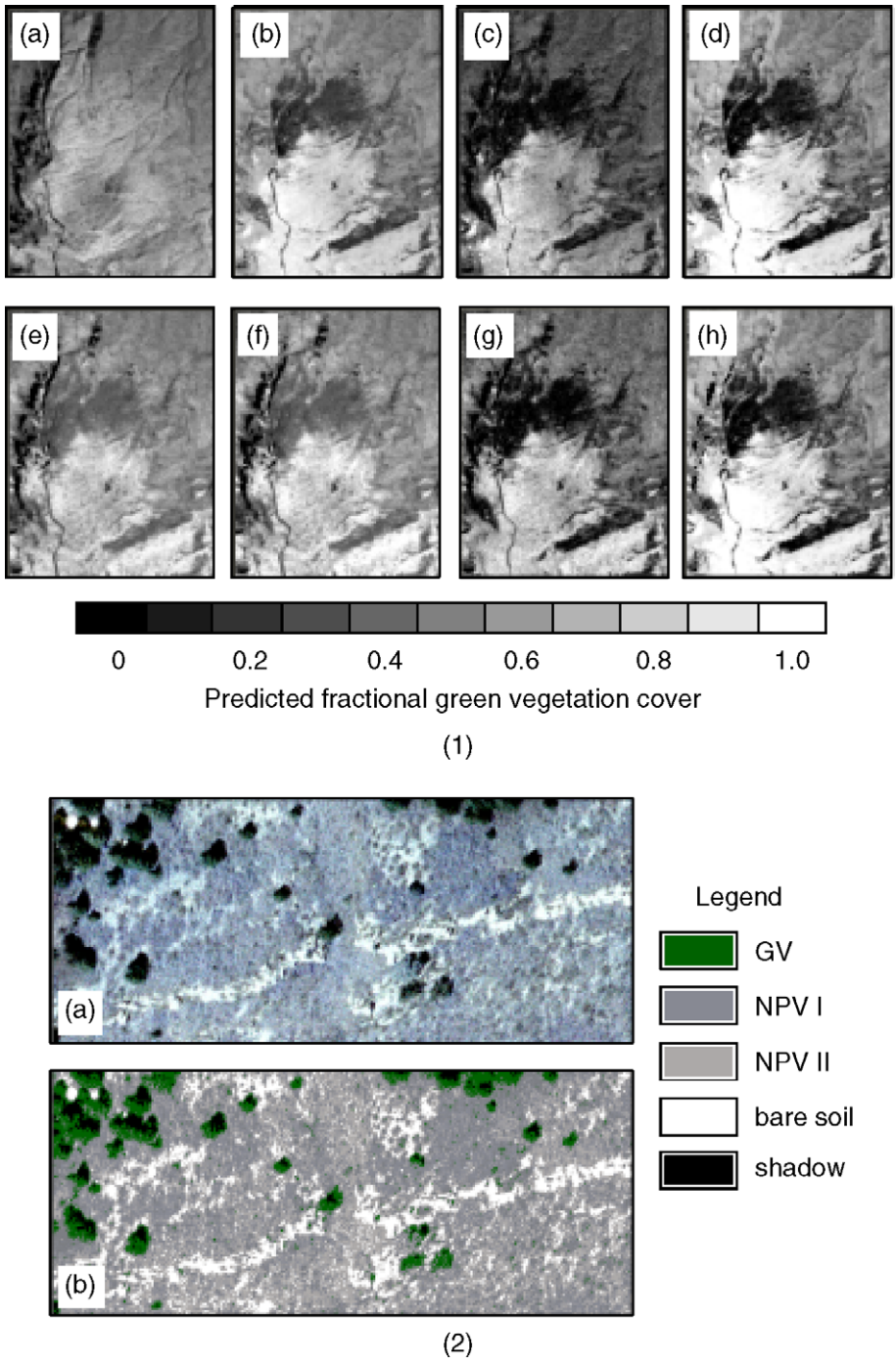

Fig. 5. Fractional green vegetation cover (f_c) and high-resolution orthoimagery for the *NPV*-dominated area delineated by the green rectangle in Fig. 1. (1) Predicted f_c: (a) unconstrained SMA3; (b) constrained SMA3; (c) unconstrained SMA4; (d) constrained SMA4; (e) NDVI-regression; (f) NDVI–SMA; (g) unconstrained SMA5; (h) constrained SMA5. Green polygons indicate *NPV*-dominated areas. (2) The high-resolution orthoimagery subset and the classified orthoimagery subset corresponding to the area delineated by the red rectangle in (1). (For interpretation of the references to colour in this figure legend, the reader is referred to the web version of this article.)

$NDVI_{veg}$ and $NDVI_{soil}$ were estimated at 0.637 and -0.054, respectively, by inversion of NDVI-regression (Fig. 7). Based on these values, NDVI–SMA was used to estimate f_c for each pixel in the ETM+ image. The relationship between actual f_c and estimated cover (Fig. 4(f)) was similar to that of NDVI-regression (Fig. 4(e)). Likewise, NDVI–SMA had significantly higher accuracy than the unconstrained SMA3 and SMA4 models, and comparable accuracy to the constrained SMA3 and SMA4 models (Table 1, Fig. 4). As with NDVI-regression, NDVI–SMA also substantially over-estimated f_c in *NPV*-dominated areas (Fig. 5) and sparsely-vegetated or barren areas with *Light Soil* background.

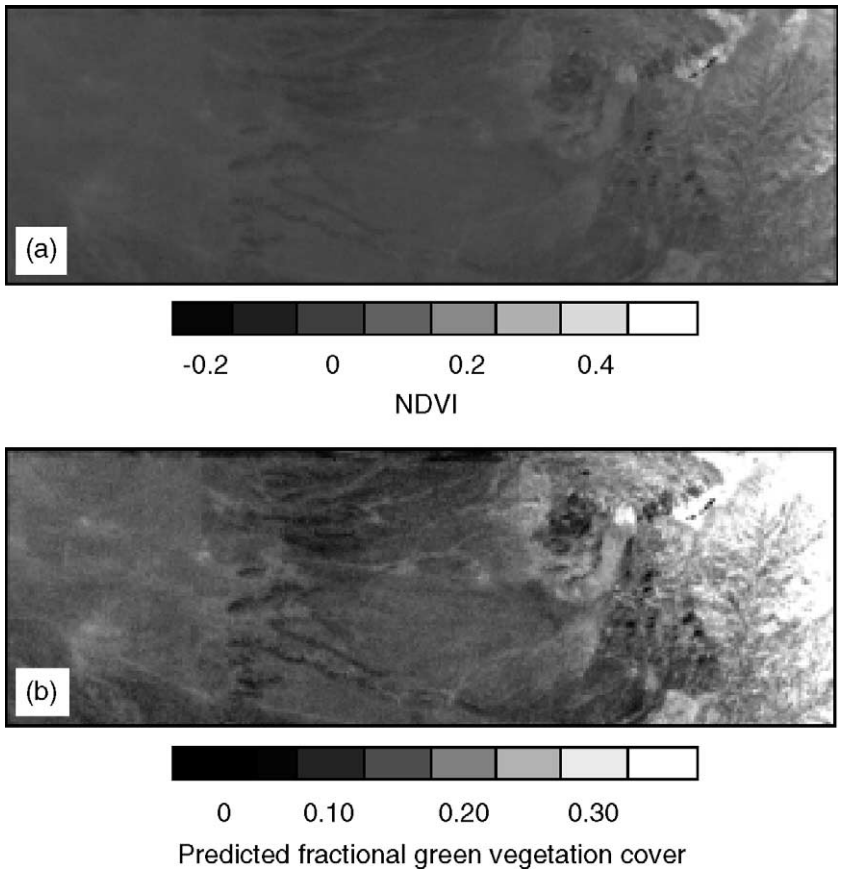

Fig. 6. NDVI values and fractional green vegetation cover (f_c) of the Landsat ETM+ subset for a sparsely-vegetated or barren area delineated by the blue rectangle in Fig. 1: (a) NDVI; (b) f_c predicted from the NDVI-regression method.

NDVI–SMA is based on the assumption that the NDVI value of a given pixel is the linear combination of NDVI values of green vegetation and bare soil. The strong, linear relation observed between $NDVI_{mixed}$ and original NDVI values (Fig. 8) shows that the linearity assumption is valid for this particular area. Thus, NDVI can be used for linear SMA in our study region. By contrast, Lobell and Asner (2004) suggested that the relation between NDVI and

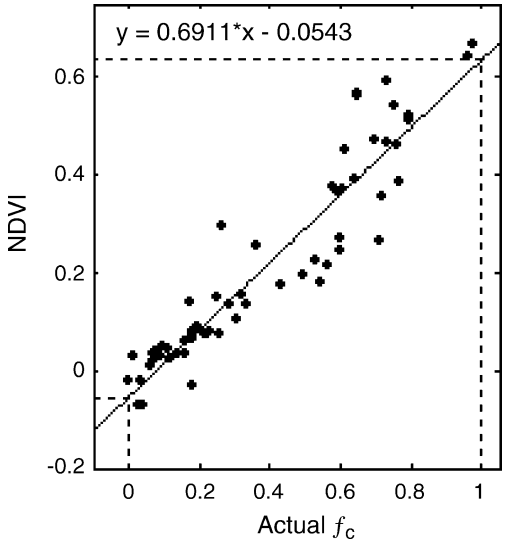

Fig. 7. Relationship between NDVI and actual fractional green vegetation cover (f_c) and estimation of $NDVI_{veg}$ and $NDVI_{soil}$ ($NDVI_{veg}=0.6367$, $NDVI_{soil}=-0.0543$).

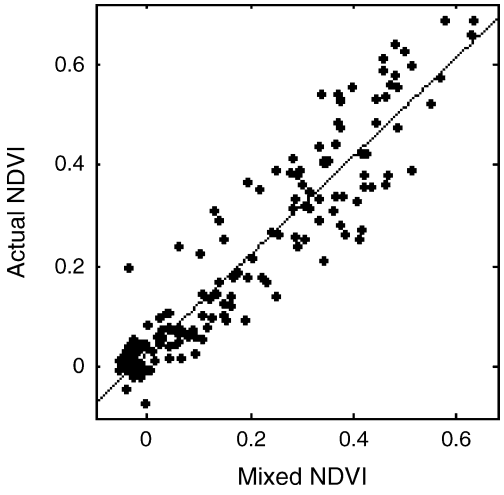

Fig. 8. Relationship between mixed NDVI ($NDVI_{mixed}$) and actual NDVI ($NDVI_{actual}$) values demonstrating the validity of the linearity assumption underlying the NDVI–SMA model ($NDVI_{actual}=0.028+0.978\times NDVI_{mixed}$; $R^2=0.88$, $p<0.0001$).

endmember fractions is not linear and thus NDVI cannot be used in linear SMA.

NDVI–SMA and NDVI-regression had similar accuracy for estimating f_c because of their mathematical similarity. NDVI–SMA (Eq. (10)) can be rewritten as:

$$f_c = \left(1/\left(\mathrm{NDVI}_{veg} - \mathrm{NDVI}_{soil}\right)\right) \times \mathrm{NDVI} - \mathrm{NDVI}_{soil}/\left(\mathrm{NDVI}_{veg} - \mathrm{NDVI}_{soil}\right). \quad (13)$$

For an established NDVI–SMA model, $1/(\mathrm{NDVI}_{veg} - \mathrm{NDVI}_{soil})$ and $\mathrm{NDVI}_{soil}/(\mathrm{NDVI}_{veg} - \mathrm{NDVI}_{soil})$ are constants. As with NDVI-regression, NDVI–SMA is also based on a linear relation between f_c and NDVI (Qi et al., 2000; Wittich & Hansing, 1995; Zeng et al., 2000). Thus, the only difference between these two models is that the coefficients are derived in different ways.

The best SMA5 models included endmembers for *Green Vegetation I, Green Vegetation II, NPV, Dark Soil*, and *Light Soil*. The accuracy of both constrained and unconstrained SMA5 models for estimating f_c were comparable to that of constrained SMA3 and SMA4, and significantly higher than that of unconstrained SMA3 and SMA4 (Table 1, Fig. 4). Both SMA5 models predicted f_c well for the full range of vegetation cover, and the two models produced almost identical accuracy. As with SMA4, SMA5 models predicted f_c well for *NPV*-dominated areas (Fig. 5) due the inclusion of the *NPV* endmember in the models.

The overall accuracy of the SMA5 models was not significantly different than the SMA4 constrained model. This is because the additional endmember (*Green Vegetation I*) in the SMA5 model represented vegetation that was only narrowly distributed in riparian areas. Despite the lack of improvement in overall accuracy, the constrained SMA5 model more accurately estimated f_c in riparian areas than the other models (Fig. 9). All other methods overestimated f_c in riparian areas (Fig. 9). This suggests that green woody vegetation and green grass cover should be represented two different endmembers because they are spectrally different, particularly in the NIR wavelength (Fig. 3).

7. Discussion

The study area is a spatially heterogeneous, arid to semi-arid environment, with strong topographically driven gradients in temperature, moisture, and productivity. Spatial variability in land-surface characteristics, and thus reflectance properties, is also produced by the patchy distribution of soil types and vegetation communities. In our results, constrained SMA3 and SMA4 models were substantially more accurate for estimating f_c than their unconstrained counterparts, suggesting that three or four endmembers are not sufficient to account for the spectral variability in the study environment. Constrained and unconstrained SMA models can produce different endmember fractions when too few or too many spectral endmembers are used (Sabol et al., 1992) because the unity constraint, when employed, forces the sum of all endmember fractions to approach 100%. The accuracy of the two SMA5 models did not differ, suggesting that, in our study system, five endmembers are adequate to spectrally characterize the non-urban landscapes. In addition, although constrained SMA3, con-

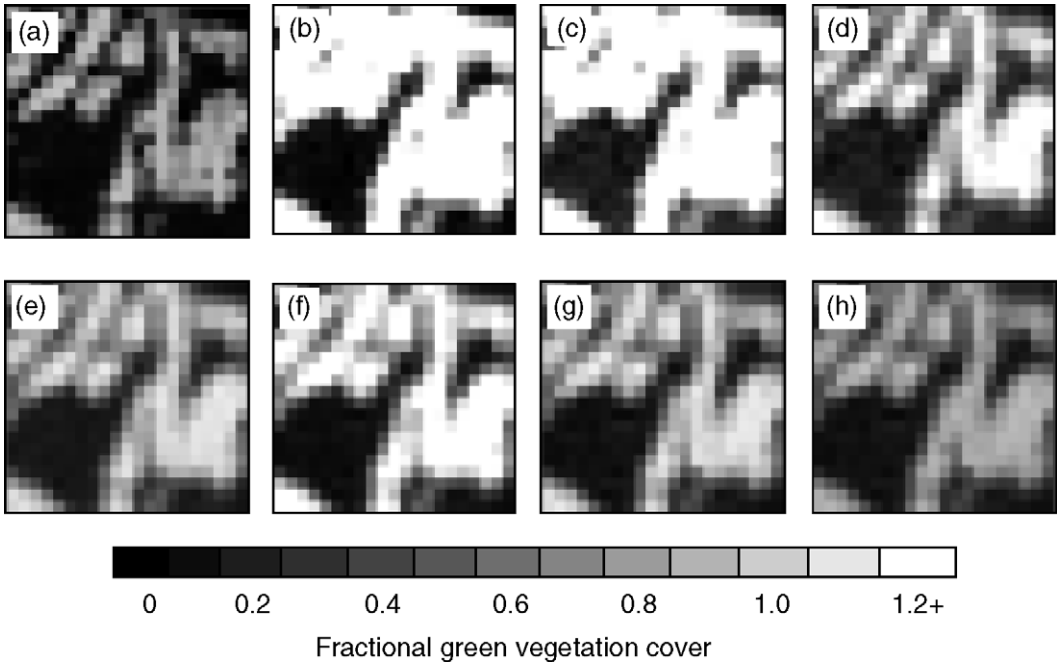

Fig. 9. Actual and predicted fractional green vegetation cover (f_c) for riparian vegetation delineated by the red rectangle in Fig. 1: (a) actual f_c derived from high-resolution orthoimagery; (b) unconstrained SMA3; (c) unconstrained SMA4; (d) unconstrained SMA5; (e) NDVI-regression; (f) constrained SMA3; (g) constrained SMA4; (h) constrained SMA5. (b)–(h) is fractional green vegetation cover (f_c) estimated from each method.

strained SMA4, and SMA5 models performed well over the study region, substantial differences in model performance were evident in the less common landscape types within the region. The constrained five endmember model better estimated f_c across the range of landscape types present. In other landscapes, for example urban areas, three endmembers have been found sufficient to account for spectral variability (Small, 2001).

The relationship between NDVI and f_c was nearly linear for our study area. This result was consistent with many studies (Hirano et al., 2004; Hurcom & Harrison, 1998; Shimabukuro et al., 1997; Wittich & Hansing, 1995), but inconsistent with strongly nonlinear relationships shown in others (Carlson & Ripley, 1997; Choudhury et al., 1994; Dymond et al., 1992; Gillies & Carlson, 1995; Lobell & Asner, 2004; Purevdorj et al., 1998). This implies that the range of f_c represented within the study region is below the level at which NDVI saturates in its response to leaf area index (LAI) (Carlson & Ripley, 1997) which may correlate with vegetation cover at the ETM+ pixel scale. Our results imply that the response of NDVI to vegetation cover in similar ecosystems, and at similar phenological stages, may also be linear. Note that the Landsat ETM+ image used in the study was acquired in early spring. Since the LAI values of coniferous forest will increase from spring through summer, the relation between NDVI and f_c may become nonlinear as the growing season progresses.

Elvidge and Lyon (1985) and Huete et al. (1985) found that greenness measures of vegetation canopies were significantly affected by soil background reflectance. Likewise, García-Haro et al. (1996) and Elmore et al. (2000) found that spectral mixture modeling was less sensitive to background soil reflectance than the NDVI-regression method. These affects were evident in our results, where we found that the NDVI-based methods were sensitive to the slightly higher NDVI values for *Light Soil* and *NPV*, relative to *Dark Soil*. As a result, f_c was overestimated in *NPV*-dominated areas and in sparsely vegetated areas with light soil background. For other areas, however, both NDVI-based methods provided good estimates of f_c.

There are several sources of uncertainty inherent in the methods compared in this analysis. First, nonlinear mixing of reflectance from sparse vegetation canopies and soil background influences the spectral observation of plants in semi-arid regions (Borel & Gerstl, 1994; Huete, 1986; Huete et al., 1985), which may impose limits on the utility of linear SMA for estimating fractional vegetation cover (Ray & Murray, 1996). Errors caused by nonlinear mixing may be minimized by nonlinear SMA models (Ju et al., 2003), artificial neural networks (Atkinson et al., 1997; Pu et al., 2003), or regression trees (DeFries et al., 1997; Yang et al., 2003).

Second, within-endmember variability in spectral signatures was assumed to be negligible, but this may not be the case. For example, Bateson et al. (2000) showed that variability in the structural and biochemical attributes of vegetation may reduce the accuracy of vegetation cover fractions from SMA. Likewise, NDVI values may vary depending on water limitation (e.g., Sandholt et al., 2002), which could lead to underestimation of f_c from both NDVI-based methods.

Third, the endmember pixels used for model development were not truly pure, in the sense that a small amount of shadow or soil background may have been included in *Green Vegetation I*, *Green Vegetation II*, and *NPV*. This is an unavoidable consequence of using image endmembers. For the NDVI–SMA model, additional sources of uncertainty relate to the sample-based estimation of NDVI endmember values for 0% and 100% f_c (i. e. $NDVI_{soi}$ and $NDVI_{veg}$) by inversion of a linear regression model.

Although our study region does not constitute a representative sample of the range of environments within the southwestern US, it is typical of much of the southwest in that it encompasses gradients among desert and semi-desert shrublands, riparian areas, and woodlands and forests of the southwestern uplands. As in much of the US southwest, the study region also includes spatial heterogeneity in vegetation form and density, and in soil background reflectance. The results of our work thus have several implications for mapping of f_c within regional-scale study areas in the US southwest.

First, NDVI-based methods for estimating f_c may be sufficient for relatively simple landscapes where there is little spectral variability within the photosynthetic and non-photosynthetic components of the surface, and where the relationship between NDVI and fractional cover is approximately linear. This implies that, within a region such as ours, improved estimates of fractional cover could be achieved by stratifying the landscape into several units prior to the development and application of separate NDVI-based models.

Second, green woody vegetation and green grass cover should be spectrally represented by two different endmembers because these two vegetation types are spectrally different, particularly in the NIR wavelength. The use of a single vegetation endmember can lead to either over- or under-estimation of f_c if both vegetation types are present. Specifically, f_c would be overestimated for green grass cover if the endmember were extracted from green woody vegetation; f_c would be underestimated for green woody cover if the endmember were extracted from green grass.

Third, larger study areas within the southwestern US may be too spectrally variable to properly characterize using only 3 or 4 endmembers. Our results suggest that 5 endmembers are more appropriate for the study area, and that NDVI can be incorporated into the Landsat ETM+ dataset to provide enough dimensionality to support the addition of a fifth endmember.

We also note that although SMA5 models had higher accuracy for estimating f_c in less common landscapes (NPV, riparian vegetation) than SMA3 and SMA4 models, the accuracy of constrained SMA3 model and constrained SMA4 model was comparable to that of SMA5 models in

other landscapes. This suggests that heterogeneous landscapes can be stratified into relatively homogeneous strata, and a spectral mixture model can be applied to each stratum separately. For each stratum, three or four endmembers may be adequate to characterize the spectral variability within the stratum. For example, Coca et al. (2004) developed the variable endmember SMA (VESMA) technique, which stratifies the study region and selects an appropriate model for each stratum. Incorporating the capacity for five endmembers with this technique may provide additional improvement in estimates of f_c. Another relatively new technique, the multiple-endmember SMA model (MESMA) (Roberts et al., 1998), may also be able to better capture the spatial variability in surface reflectance in heterogeneous landscapes than three- or four-endmember mixture models.

8. Conclusions

Our results suggest that simple methods for estimating fractional green vegetation cover from NDVI are suitable for some landscapes in arid and semi-arid regions. However, NDVI-based methods are sensitive to soil background reflectance. In sparsely vegetated areas, NDVI-based methods are affected by non-photosynthetically active scene components (e.g. substrate or senescent vegetation) that produce high NDVI values. In these cases, fractional green vegetation cover is typically overestimated.

Model limitations within certain landscape types, and comparison of constrained vs. unconstrained models, suggested that the most effective approach for estimating fractional green vegetation cover within this region should be based on five endmembers. Three or four endmembers may be inadequate to spectrally characterize large, heterogeneous landscapes. We found that, by using NDVI as an additional data dimension along with the reflectance bands of ETM+ data, a five-endmember model performed as well as any other model, and better estimated fractional green vegetation cover in riparian areas due to the inclusion of the fifth endmember.

We also note that constrained SMA3 model, constrained SMA4 model, and both SMA5 models all produced comparable overall (i. e. region-wide) accuracies in our study region although SMA5 models had higher accuracy in less common landscapes (NPV, riparian vegetation). This indicates that heterogeneous landscapes can be stratified into relatively homogeneous strata, and a spectral mixture model can be applied to each stratum separately. For each stratum, three or four endmembers may be adequate to characterize the spectral variability within the stratum. The use of five or more endmembers within each stratum may further improve the representation of the spectral variability of land-cover types within the stratum and thus potentially improve the accuracy for estimating fractional green vegetation cover.

Acknowledgements

This research was supported by NASA through a Graduate Student Fellowship in Earth System Science awarded to J. Xiao (Fellowship grant number: 5-35837). We thank M.R. Majid and Dr. C. Song for helpful discussion about high-resolution orthoimagery and atmospheric correction. Landsat ETM+ data, high-resolution orthoimagery, and topographic maps were provided by Global Land Cover Facility, U.S. Geological Survey EROS Data Center, and the New Mexico Resource Geographic Information System (RGIS), respectively. We also thank the four anonymous reviewers for their valuable comments on an earlier version of the manuscript.

References

Adams, J. B., Smith, M. O., & Johnson, P. E. (1986). Spectral mixture modeling: A new analysis of rock and soil types at the Viking Lander 1 site. *Journal of Geophysical Research*, *91*, 8098–8112.

Adams, J. B., Sabol, D. E., Kapos, V., Filho, R. A., Roberts, D. A., Smith, M. O., et al. (1995). Classification of multispectral images based on fractions of endmembers: Application to land-cover change in the Brazilian Amazon. *Remote Sensing of Environment*, *52*, 137–154.

Asner, G. P., & Heidebrecht, K. B. (2002). Spectral unmixing of vegetation, soil and dry carbon cover in arid regions: Comparing multispectral and hyperspectral observations. *International Journal of Remote Sensing*, *23*, 3939–3958.

Asrar, G., Fuchs, M., Kanemasu, E. T., & Hatfield, J. L. (1984). Estimating of absorbed photosynthetic radiation and leaf area index from spectral reflectance in wheat. *Agronomy Journal*, *76*, 300–306.

Atkinson, P. M., Cutler, M. E. J., & Lewis, H. (1997). Mapping a sub-pixel proportional land cover with AVHRR imagery. *International Journal of Remote Sensing*, *18*, 917–935.

Bateson, C. A., Asner, G. P., & Wessman, C. A. (2000). Endmember bundles: A new approach to incorporating endmember variability into spectral mixture analysis. *IEEE Transactions on Geoscience and Remote Sensing*, *38*, 1083–1094.

Boardman, J. W., Kruse, F. A., & Green, R. O. (1995). Mapping target signatures via partial unmixing of AVIRIS data. Summaries of the Fifth JPL Airborne Earth Science Workshop, 23–26 January, Pasadena, California. *JPL Publications*, *Vol. 95-1* (pp. 23–26). Pasadena, California: Jet Propulsion Laboratory.

Borel, C. C., & Gerstl, S. A. W. (1994). Nonlinear spectral mixing models for vegetative and soil surfaces. *Remote Sensing of Environment*, *47*, 403–416.

Carlson, T. N., & Ripley, D. A. (1997). On the relation between NDVI, fractional vegetation cover, and leaf area index. *Remote Sensing of Environment*, *62*, 241–252.

Chavez Jr., P. S. (1989). Radiometric calibration of Landsat Thematic Mapper multispectral images. *Photogrammetric Engineering and Remote Sensing*, *55*, 1285–1294.

Choudhury, B. J., Ahmed, N. U., Idso, S. B., Reginato, R. J., & Daughtry, C. S. T. (1994). Relations between evaporation coefficients and vegetation indices studied by model simulations. *Remote Sensing of Environment*, *50*, 1–17.

Coca, F. C., García-Haro, F. J., Gilabert, M. A., & Meliá, J. (2004). Vegetation cover seasonal changes assessment from TM imagery in a semi-arid landscape. *International Journal of Remote Sensing*, *25*, 3451–3476.

Deardorff, J. W. (1978). Efficient prediction of ground temperature and moisture with inclusion of a layer of vegetation. *Journal of Geophysical Research*, *83*, 1889–1903.

DeFries, R., Hansen, M., Steininger, M., Dubyah, R., Sohlberg, R., & Townshend, J. (1997). Subpixel forest cover in Central Africa from multisensor, multitemporal data. *Remote Sensing of Environment*, *60*, 228–246.

Dymond, J. R., Stephens, P. R., Newsome, P. F., & Wilde, R. H. (1992). Percentage vegetation cover of a degrading rangeland from SPOT. *International Journal of Remote Sensing*, *13*, 1999–2007.

Earth Data Analysis Center. (1991). 1:1,000,000 General vegetation map of New Mexico. Publisher: Earth Data Analysis Center, Albuquerque, New Mexico.

Elmore, A. J., Mustard, J. F., Manning, S. J., & Lobell, D. B. (2000). Quantifying vegetation change in semiarid environments: Precision and accuracy of spectral mixture analysis and the normalized difference vegetation index. *Remote Sensing of Environment*, *73*, 87–102.

Elvidge, C. D., & Lyon, R. J. P. (1985). Influence of rock soil spectral variation on the assessment of green biomass. *Remote Sensing of Environment*, *17*, 265–279.

Foody, G. M. (1996). Approaches for the production and evaluation of fuzzy land cover classifications from remotely-sensed data. *International Journal of Remote Sensing*, *62*, 491–499.

Foody, G. M., Campbell, N. A., Trodd, N. M., & Wood, T. F. (1992). Derivation and applications of probabilistic measures of class membership from the maximum-likelihood classification. *Photogrammetric Engineering and Remote Sensing*, *58*, 1335–1341.

García-Haro, F. J., Gilabert, M. A., & Melia, J. (1996). Linear spectral mixture modeling to estimate vegetation amount from optical spectral data. *International Journal of Remote Sensing*, *17*, 3373–3400.

Gillies, R. R., & Carlson, T. N. (1995). Thermal remote sensing of surface soil water content with partial vegetation cover for incorporation into climate models. *Journal of Applied Meteorology*, *34*, 745–756.

Graetz, R. D., & Gentle, M. R. (1982). The relationship between reflectance in the Landsat wavebands and the composition of an Australian semi-arid shrub rangeland. *Photogrammetric Engineering and Remote Sensing*, *48*, 1721–1730.

Gutman, G., & Ignatov, A. (1998). The derivation of the green vegetation fraction from NOAA/AVHRR data for use in numerical weather prediction models. *International Journal of Remote Sensing*, *19*, 1533–1543.

Häme, T., Stenberg, P., Anderson, K., Rauste, Y., Kennedy, P., Folving, S., et al. (2001). AVHRR-based forest proportion map of the Pan-European area. *Remote Sensing of Environment*, *77*, 76–91.

Heinz, D. C., & Chang, C. I. (2001). Fully constrained least squares linear spectral mixture analysis method for material quantification in hyperspectral imagery. *IEEE Transactions on Geoscience and Remote Sensing*, *39*, 529–545.

Hirano, Y., Yasuoka, Y., & Ichinose, T. (2004). Urban climate simulation by incorporating satellite-derived vegetation cover distribution into a mesoscale meteorological model. *Theoretical and Applied Climatology*, *79*, 175–184.

Hoffmann, W. A., & Jackson, R. (2000). Vegetation-climate feedbacks in the conversion of tropical savanna to grassland. *Journal of Climate*, *13*, 1593–1602.

Huete, A. R., Jackson, R. D., & Post, D. F. (1985). Spectral response of a plant canopy with different soil backgrounds. *Remote Sensing of Environment*, *17*, 37–53.

Huete, A. R. (1986). Separation of soil-plant spectral mixtures by factor analysis. *Remote Sensing of Environment*, *19*, 237–251.

Hurcom, S. J., & Harrison, A. R. (1998). The NDVI and spectral decomposition for semi-arid vegetation abundance estimation. *International Journal of Remote Sensing*, *19*, 3109–3125.

Ju, J., Kolaczyk, E. D., & Gopal, S. (2003). Gaussian mixture discriminant analysis and sub-pixel land cover characterization in remote sensing. *Remote Sensing of Environment*, *84*, 550–560.

Lobell, D. B., & Asner, G. P. (2004). Cropland distributions from temporal unmixing of MODIS data. *Remote Sensing of Environment*, *93*, 412–422.

Markham, B. L., & Barker, J. L. (1987). Radiometric properties of U.S. processed Landsat MSS data. *Remote Sensing of Environment*, *22*, 39–71.

McDonald, A. J., Gemmell, F. M., & Lewis, P. E. (1998). Investigation of the utility of spectral vegetation indices for determining information on coniferous forests. *Remote Sensing of Environment*, *66*, 250–272.

McIver, D. K., & Friedl, M. A. (2002). Using prior probabilities in decision-tree classification of remotely sensed data. *Remote Sensing of Environment*, *81*, 253–261.

Moran, M. S., Jackson, R. D., Slater, P. N., & Teillet, P. M. (1992). Evaluation of simplified procedures for retrieval of land surface reflectance factors from satellite sensor output. *Remote Sensing of Environment*, *41*, 169–184.

Myneni, R. B., Hall, F. G., Sellers, P. J., & Marshak, A. L. (1995). The interpretation of spectral vegetation indexes. *IEEE Transactions on Geoscience and Remote Sensing*, *33*, 481–486.

Nemani, R., & Running, S. W. (1996). Global vegetation cover changes from coarse resolution satellite data. *Journal of Geophysical Research*, *101*, 7157–7162.

Oki, K., Oguma, H., & Sugita, M. (2002). Subpixel classification of alder trees using multitemporal Landsat Thematic Mapper imagery. *Photogrammetric Engineering and Remote Sensing*, *68*, 77–82.

Pech, R. P., Graetz, R. D., & Davis, A. W. (1986). Reflectance modeling and the derivation of vegetation indices for an Australian semi-arid shrubland. *International Journal of Remote Sensing*, *7*, 389–403.

Peterson, S. H., & Stow, D. A. (2003). Using multiple image endmember spectral mixture analysis to study chaparral regrowth in southern California. *International Journal of Remote Sensing*, *24*, 4481–4504.

Price, J. C. (1987). Special issue on radiometric calibration of satellite data. *Remote Sensing of Environment*, *22*, 1–158.

Purevdorj, T., Tateishi, R., Ishiyama, T., & Honda, Y. (1998). Relationships between percent vegetation cover and vegetation indices. *International Journal of Remote Sensing*, *19*, 3519–3535.

Pu, R., Xu, B., & Gong, P. (2003). Oakwood crown closure estimation by unmixing Landsat TM data. *International Journal of Remote Sensing*, *24*, 4433–4445.

Qi, J., Marsett, R. C., Moran, M. S., Goodrich, D. C., Heilman, P., Kerr Y. H., et al. (2000). Spatial and temporal dynamics of vegetation in the San Pedro River basin area. *Agricultural and Forest Meteorology*, *105*, 55–68.

Rashed, T., Weeks, J. R., Roberts, D., Rogan, J., & Powell, R. (2003). Measuring the physical composition of urban morphology using multiple endmember spectral mixture models. *Photogrammetric Engineering and Remote Sensing*, *69*, 1011–1020.

Ray, T. W., & Murray, B. C. (1996). Nonlinear spectral mixing in desert vegetation. *Remote Sensing of Environment*, *55*, 59–64.

Roberts, D. A., Gardner, M., Church, R., Ustin, S., Scheer, G., & Green, R. O. (1998). Mapping chaparral in the Santa Monica mountains using multiple endmember spectral mixture models. *Remote Sensing of Environment*, *65*, 267–279.

Sabol, D. E., Adams, J. B., & Smith, M. O. (1992). Quantitative sub-pixel spectral detection of targets in multispectral images. *Journal of Geophysical Research*, *97*, 2659–2672.

Sandholt, I., Rasmussen, K., & Andersen, J. (2002). A simple interpretation of the surface temperature/vegetation index space for assessment of surface moisture status. *Remote Sensing of Environment*, *79*, 213–224.

Schimel, D. S., House, J. I., Hibbard, K. A., Bousquet, P., Ciais P., et al. (2001). Recent patterns and mechanisms of carbon exchange by terrestrial ecosystems. *Nature*, *414*, 169–172.

Shimabukuro, Y. E., Carvalho, V. C., & Rudorff, B. F. T. (1997). NOAA-AVHRR data processing for the mapping of vegetation cover. *International Journal of Remote Sensing*, *18*, 671–677.

Shoshany, M., & Svoray, T. (2002). Multidate adaptive unmixing and its application to analysis of ecosystem transitions along a climatic gradient. *Remote Sensing of Environment*, *82*, 5–20.

Small, C. (2001). Estimation of urban vegetation abundance by spectral mixture analysis. *International Journal of Remote Sensing*, *22*, 1305–1334.

Small, C. (2003). High spatial resolution spectral mixture analysis of urban reflectance. *Remote Sensing of Environment*, *88*, 170–186.

Smith, M. O., Ustin, S. L., Adams, J. B., & Gillespie, A. R. (1990). Vegetation in deserts: I. A regional measure of abundance from multispectral images. *Remote Sensing of Environment*, *31*, 1–26.

Strahler, A. H., Woodcock, C. E., & Smith, J. A. (1986). On the nature of models in remote-sensing. *Remote Sensing of Environment*, *20*, 121–139.

Teillet, P. M., & Fedosejevs, G. (1995). On the dark target approach to atmospheric correction of remotely sensed data. *Canadian Journal of Remote Sensing*, *21*, 373–387.

Theseira, M. A., Thomas, G., & Sannier, C. A. D. (2002). An evaluation of spectral mixture modeling applied to a semi-arid environment. *International Journal of Remote Sensing*, *23*, 687–700.

Tompkins, S., Mustard, J. F., Pieters, C. M., & Forsyth, D. W. (1997). Optimization of endmembers for spectral mixture analysis. *Remote Sensing of Environment*, *59*, 472–489.

Tueller, P. T. (1987). Remote sensing science applications in arid environments. *Remote Sensing of Environment*, *23*, 143–154.

Ward, R. C., & Robinson, M. (2000). *Principles of Hydrology* (4th edition). McGraw hill. 450 pp.

Wittich, K. P., & Hansing, O. (1995). Area-averaged vegetative cover fraction estimated from satellite data. *International Journal of Biometeorology*, *38*, 209–215.

Wu, C., & Murray, A. T. (2003). Estimating impervious surface distribution by spectral mixture analysis. *Remote Sensing of Environment*, *84*, 493–505.

Yang, L., Huang, C., Homer, C. G., Wylie, B. K., & Coan, M. J. (2003). An approach for mapping large-area impervious surfaces: Synergistic use of Landsat-7 ETM+ and high resolution imagery. *Canadian Journal of Remote Sensing*, *29*, 230–240.

Zeng, X., Dickinson, R. E., Walker, A., & Shaikh, M. (2000). Derivation and evaluation of global 1-km fractional vegetation cover data for land modeling. *Journal of Applied Meteorology*, *39*, 826–839.